Multi-objective optimization of supersonic separator for gas removal and carbon capture using three-field two-phase flow model and non-dominated sorting Genetic Algorithm-II (NSGA-II)

Separation and Purification Technology 358 (2025) 130363

Contents lists available at ScienceDirect

Separation and Purification Technology

journal homepage: www.elsevier.com/locate/seppur

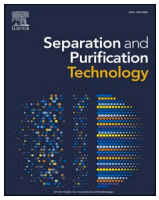

Multi-objective optimization of supersonic separator for gas removal and carbon capture using three-field two-phase flow model and non-dominated sorting Genetic Algorithm-II (NSGA-II)

Hongbing Ding [a], Guangchen Zhang [a], Shiwei Wang [a,b], Yu Zhang [a], Yan Yang [c,*], Chuang Wen [d,*]

[a] Tianjin Key Laboratory of Process Measurement and Control, School of Electrical and Information Engineering, Tianjin University, Tianjin 300072, China
[b] School of Mechanical and Electrical Engineering, Huainan Normal University, Huainan 232038, China
[c] Faculty of Environment, Science and Economy, University of Exeter, Exeter EX4 4QF, United Kingdom
[d] School of the Built Environment, University of Reading, Reading RG6 6AH, United Kingdom

ARTICLE INFO

Editor: S Yi

Keywords:
Separation Efficiency
Supersonic separator
Multi-objective Optimization Method
Gas–liquid three-field two-phase CFD model
Non-dominated Sorting Genetic Algorithm-II
Cost analysis

ABSTRACT

Supersonic separator is an efficient technology for gas removal and carbon capture. To enhance its performance, many researchers have studied its structure; however, existing studies have primarily used traditional computational fluid dynamics (CFD) models for single-objective structural optimization of the separator's separation performance. However, in the supersonic separators, separation efficiency and pressure-loss ratio are the most important and conflicting performance parameters, and evaluating separation performance in isolation from either one is incomplete. In the present study, we develop a gas–liquid two-phase three-field CFD model considering liquid films. This mathematical model is combined with the non-dominated Sorting Genetic Algorithm-II (NSGA-II) for multi-objective optimization of the coupled multiple structural parameters with the objective of the separation efficiency and pressure-loss ratio. The results indicate that the maximum relative errors between simulated and predicted values for the four Pareto optimal solutions in computing pressure loss ratio and separation efficiency are 5.4% and 5.3%, respectively. The optimized solutions achieve the maximum reduction in pressure loss ratio of 28.3% at the same 90% separation efficiency compared to the original structure.

1. Introduction

Currently, global warming and environmental pollution issues are becoming increasingly serious [1], and addressing climate change and reducing pollution has become a mainstream global task [2]. Therefore, countries around the world are actively seeking clean energy alternatives to fossil fuels, and one important renewable energy sources is natural gas [3]. In fact, natural gas produced by current extraction technologies inevitably contains liquid droplets, water vapor, CO_2, and other components [4]. Before gathering and transportation, it is essential to remove components that may affect transportation safety and efficiency, particularly water and CO_2 [5]. Water liquid reacts with heavier hydrocarbons to form natural gas hydrates, which can block pipelines and valves, reducing transportation efficiency [6], reducing transportation capacity and causing unnecessary energy consumption. Additionally, water vapor and acidic gases like CO_2 can form carbonic acid, which corrodes pipelines, shortening their service life and posing safety risks such as leaks or explosions [7]. For offshore natural gas extraction technologies rich in CO_2, which are both costly and technically challenging, this issue requires special attention [8]. Therefore, employing more cost-effective and energy-efficient natural gas dehydration and carbon capture processes to effectively remove components such as H_2O and CO_2, which affect equipment operation, pipeline safety, and transportation efficiency, is crucial for the development of the natural gas industry [9].

Typically, gravitational sedimentation and swirl separation methods, based on density differences between components, are used to remove impurities such as liquid droplets from natural gas feed [10]. Commonly used natural gas dehydration and carbon capture technologies include membrane and absorption, and adsorption processes. Each technology has its unique material requirements, specific application environments, operational conditions, and distinct advantages and disadvantages. The membrane separation method uses the difference in partial pressure and

* Corresponding authors.
E-mail addresses: y.yang7@exeter.ac.uk, yanyang2021@outlook.com (Y. Yang), c.wen@reading.ac.uk (C. Wen).

https://doi.org/10.1016/j.seppur.2024.130363
Received 15 August 2024; Received in revised form 31 October 2024; Accepted 31 October 2024
Available online 2 November 2024

Nomenclature

Term

$\dot{m}$	Mass source term, kg m^{-3} s^{-1}
U	Momentum source term, Pa/m
Q	Energy source term, J kg^{-1} s^{-1}
p	Pressure, Pa
E	Energy of the gas phase, J kg^{-1}
T	Temperature, K
u	Velocity, m/s
$\overrightarrow{g}$	Acceleration of gravity, m/s^2
C_c	drag coefficient, –
$\dot{Y}$	mass fraction, –
m_p	Droplet mass, kg
l	Mean free path of the molecule, mm
h	Enthalpy, J kg^{-1}
C_{phase}	Phase change constant, –
R	Radius, mm
S_s	Supersaturation, –
D	Distance,μm
q	Mass flow rate, kg s^{-1}
d	Diameter, mm
A_p	Surface area, m^2
V_{cell}	Volume of the control volume, m^3
Δt	Time step, s
a_i	Heat transfer coefficient, W/m K^{-1}
R_v	Specific gas constant, J kg^{-1} K^{-1}
RH	Humidity, –
L	Length, mm
T_r	Droplet surface temperature, K
L_1	Length of convergent section, mm
$R_{hub,in}$	Radius of hub at the inlet, mm
$R_{hub,t}$	Radius of hub at the throat, mm
AR	Nozzle area expansion ratio, –

Greek

ρ	Density, kg m^{-3}
α	Volume fraction, –
μ	Dynamic viscosity, Pa s
$\overline{\overline{\tau}_{eff}}$	Stress tensor, Pa
δ	film thickness, μm
γ	Pressure loss ratio, –
η	Separation efficiency, –
σ	Surface tension, N/m

Subscripts

c	Critical
p	Droplet
sur	Film surface
w	Wall
f	Film
m	Film half-depth
g	Gas
l	Liquid
i	Species
v	Vapor
sat	Saturation vapor
de	Droplet deposition
se	Liquid film separation
st	Liquid film stripping
in	Inlet
out	Outlet
Φ	Substances to be separated
t	Throat

Superscript

*	Stagnant state

Acronyms

UDF	User-defined functions
MOOM	Multi-objective optimization method
SS	Supersonic separator
CFD	Computational fluid dynamics
OLHS	Optimal Latin Hypercube Sampling
RSM	Response surface model
DOE	Design of experiment
GA	Genetic algorithm
NSGA-II	Non-dominated Sorting Genetic Algorithm-II
MOOM	Multi-objective optimization method
DEG	Diethylene glycol
TEG	Triethylene glycol process
MEA	Monoethanolamine
DEA	Diethanolamine
TCOP	Total cost of production
VCOP	Variable cost of production
FCOP	Fixed cost of production
ACC	Annual capital cost

concentration of the components to be separated on both sides of the permeable membrane to achieve separation [11]. Its separation capability depends on the material of the permeable membrane. This method theoretically has a good separation effect, but it is difficult to implement, and the maintenance cost and difficulty are very high. For absorption dehydration, chemical solvents, such as diethylene glycol (DEG) and triethylene glycol (TEG), dissolve water vapor from the gas stream [12]. These solvents have a high affinity for water and can effectively remove moisture from natural gas. Hot potassium carbonate and Amine absorption method (such as monoethanolamine (MEA), diethanolamine (DEA), and methyl diethanolamine (MDEA)) can react chemically with CO_2 in natural gas, absorb CO_2 into the solution, and achieve efficient carbon capture [13]. Meanwhile, Physical solvents such as Selexol and Rectisol, based on the physical solubility of CO_2 in the solvent, It offers advantages such as high CO_2 absorption capacity, low energy consumption for regeneration, and good stability under process conditions [14]. The adsorption method uses solid adsorbents (such as molecular sieves and activated carbon) to selectively adsorb H_2O and CO_2 from natural gas, achieving dehydration and carbon capture. Once the adsorbent is saturated, it can be regenerated through heating or pressure reduction [15].

Different from the above separation technologies, the emerging supersonic separator (SS) technology based on the expansion condensation and swirl separation principle can not only achieve efficient dehydration and carbon capture, but also has outstanding advantages that other processes do not have, such as safety, energy saving, low cost, small size, and flexible structure, and it has very high application value and commercial prospects [16].

Brigagão et al. [17] introduced a new pre-purification unit that uses a supersonic separator to remove moisture from the air. This technology can significantly improve energy efficiency and the overall performance of the system. Interlenghi et al. [18] proposed using a supersonic separator as a novel air dehydration device in microgravity environments. This device can reduce the thermal load of primary and secondary cooling loops, has a self-cleaning function, and can sterilize air through supersonic normal shocks, providing support for environmental control and life support systems inside spacecraft. Teixeira et al. [19] used a supersonic separator to recover hydrate inhibitors and adjust the

water dew point, thereby promoting the dehydration of offshore natural gas. Bian et al. [20] used simulations to study the internal flow field characteristics and separation performance of supersonic separators when dehydrating offshore wet natural gas. Cao et al. [21] designed a novel supersonic separator with an elliptical center body, analyzed the dew point drop and adaptability at the inlet and outlet, and then evaluated its dehydration performance.

Arinelli et al. conducted studies on the use of supersonic separators, first addressing CO_2 capture from ultra-rich CO_2 natural gas, demonstrating high efficiency in processing gas with over 60% CO_2 [22], and later applying supersonic separators to convert CO_2 into methanol, improving both methanol conversion efficiency and the economic viability of the separation system [23]. Wiesberg et al. [24] studied the performance of supersonic separators for offshore natural gas decarbonization and compared it with membrane permeation methods, finding that the overall performance of the supersonic separator is superior. Teixeira et al. [25] developed a post-combustion carbon capture device using a supersonic separator, which reduced carbon emissions by approximately 43%. Lakzian et al. [26] conducted a detailed study on the phase change process inside a supersonic separator, further investigating the condensation and removal of carbon dioxide, exploring the potential of this technology for carbon capture.

It is worth noting that the natural gas supersonic dehydration process and the carbon capture process are quite similar [23,27]. Therefore, this paper only takes the natural gas supersonic dehydration process as an example to explain its basic process cycle in detail. A typical two-stage natural gas dehydration process using a supersonic separator is shown in Fig. 1. The raw natural gas first passes through a primary SS, where the liquid droplets and a small amount of vapor in the natural gas are separated under conditions of small pressure loss [28]. The gas-liquid mixture discharged from the liquid outlet is then separated by a gas-liquid separator [29], with the separated liquid being discharged and the gas returning to the gas phase outlet of the primary SS. The natural gas flowing out from primary SS is pressurized by a compressor, then cooled by heat exchangers [30], and subsequently enters the secondary SS for separation. The liquid outlet of the secondary SS releases a gas-liquid mixture, which is then separated by a low-temperature separator, with the separated liquid being discharged and the gas returning to the gas outlet of the secondary SS. The purified low-temperature natural gas is further heat-exchanged with the high-temperature natural gas mixture at the front-end secondary SS inlet and then transported outward.

The specific functions of the primary SS and the secondary SS are not entirely the same. The primary SS is designed for initial separation, effectively removing the liquid droplets from raw natural gas with low pressure loss ratio. The Secondary SS is used for finer separation, aiming to separate as much water vapor as possible from the fluid, with relatively high-pressure loss ratio and energy consumption. It can be concluded that the SS serves two crucial functions [31]: cryogenic refrigeration and gas–liquid swirling separation. As depicted in Fig. 2, it can be delineated into four primary parts: the swirl generator, Laval nozzle, gas-liquid separation section, and diffuser, structurally. Upon entering the SS, the mixture first enters the swirl generator, where the rotational flow field is generated due to the guiding action of the blades. Subsequently, the fluid enters the convergent section of the Laval nozzle, where the velocity increases while the temperature and pressure decrease sharply [32]. As fluid reaches the throat, the velocity reaches supersonic levels. Moreover, due to the low temperature and pressure at this point, water vapor becomes supersaturated and begins to condense, forming liquid film and droplets [33]. Then liquid film flows out of liquid outlet, while gas enters diffuser to restore temperature and pressure [34].

Fig. 2 also presents a schematic diagram of the condensation process, which can be categorized into homogeneous condensation and heterogeneous condensation [35]. Homogeneous condensation occurs when water vapor molecules spontaneously aggregate to form condensation nuclei, while heterogeneous condensation involves condensation nuclei introduced from the external environment [36]. Afterwards, in a low-temperature environment, more and more water vapor will accumulate around the condensation nuclei, promoting the growth of condensation nuclei [33]. Eventually, they develop into larger-sized liquid droplets, which, under the influence of swirling flow, will be thrown onto the wall surface. Then they deposit and form liquid film [37]. Homogeneous condensation, compared to heterogeneous condensation, accounts for a very small proportion [38]. Therefore, it is often neglected in practical analysis.

Within the swirling flow of three-field (gas, droplets, liquid film) and two-phase (gas, liquid) in SS, intricate heat and mass transfer processes occur among the three fields. These include non-equilibrium condensation between gas and droplets, phase transition between gas and liquid film, deposition, and entrainment between droplets and liquid film, among others [39]. Therefore, it is imperative to establish a gas-liquid three-field two-phase CFD model for swirling flow to elucidate its flow mechanism.

The supersonic separator is a highly efficient tool that can be used for gas removal and carbon capture, and its structure significantly affects its performance. Therefore, many researchers have studied its structure to improve the performance of supersonic separators. However, creating a physical model of a supersonic separator is challenging, so most existing studies use CFD simulations to examine the impact of structure on performance. Thus, establishing a CFD model that can accurately simulate the complex mass and heat transfer phenomena inside a supersonic separator is crucial for optimizing its structure.

The Euler model is a commonly used CFD model for studying structural sensitivity. Hu et al. [40] investigated the flow characteristics of a supersonic separator with a return channel, studying the effects of the return channel diameter and insertion depth on separation efficiency. The optimal dimensions were found to be a return channel diameter of 7 mm and an insertion depth of 30 mm. Cao et al. [21] used the Euler model to study the separation performance of a supersonic separator with an internal annular nozzle. Wen et al. [41] used the Euler model to study the effect of different types of diffusers on the gas flow

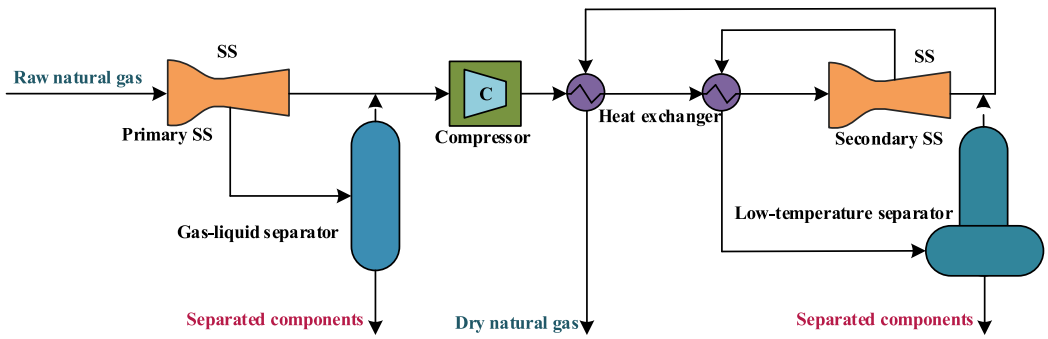

Fig. 1. Natural gas dehydration process diagram.

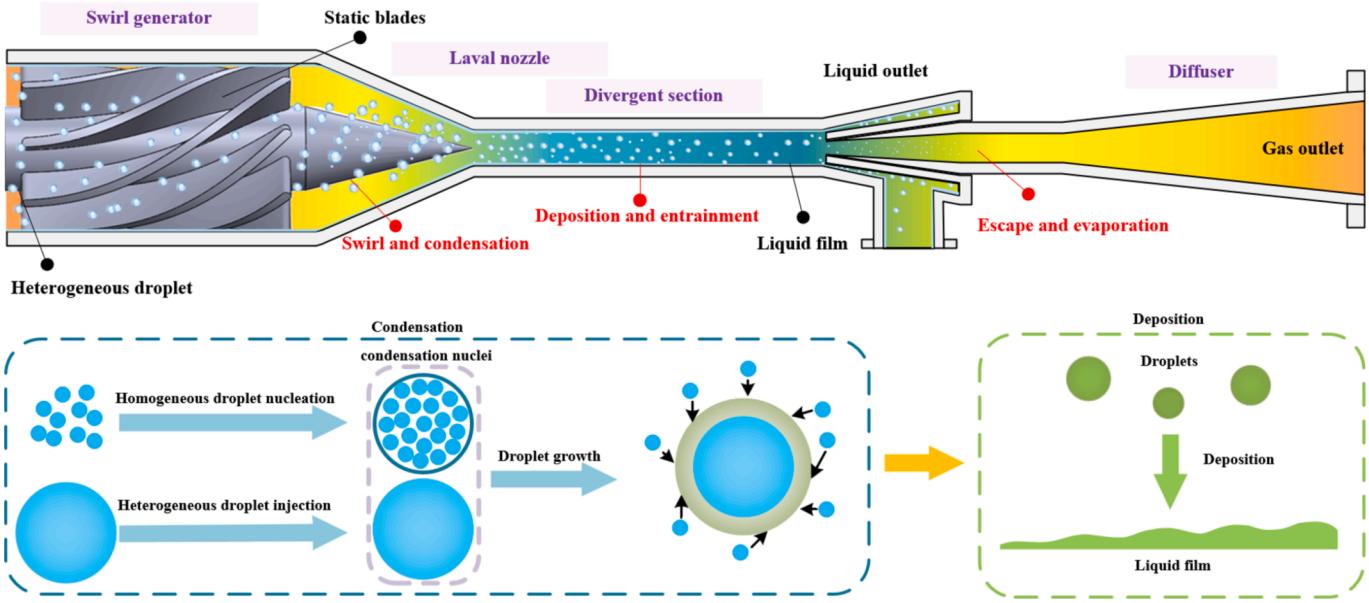

Fig. 2. Typical structure of SS and schematic diagram of condensation and deposition process.

characteristics inside the supersonic separator, and found that the conical diffuser performed best. Majidi et al. [42] used the Euler model to study the influence of the swirl section and liquid outlet on the performance of the supersonic separator.

Building on the Euler model, some researchers have considered the droplet condensation process and proposed the Euler-Euler (E-E) model and the Euler-Lagrange (E-L) model. The E-L model provides more accurate simulations of discrete droplets. Wen et al. [43] used the E-L model to study the impact of the blade-to-pipe diameter ratio on separation performance, finding that when the diameter ratio was 0.67, the droplet separation efficiency reached 70%. Yang et al. [44] used the E-L model to investigate the effect of separator length on separation efficiency, discovering that when the separator length was 16–20 times the throat diameter, a relatively high separation efficiency could be achieved. Chen et al. [45] employed the E-L solver to investigate the influence of drainage sizes on the separation efficiency.

In summary, all existing studies are based on numerical models without considering the liquid film, targeting single or multiple relatively independent structural parameters. A detailed optimization of multiple coupled structural parameters targeting two performance parameters, separation efficiency and pressure loss ratio, have not performed. However, in the SS, separation efficiency and pressure-loss ratio are the most important and conflicting performance parameters, and evaluating separation performance in isolation from either one is incomplete. Therefore, in this paper, a gas-liquid two-phase three-field CFD model considering a liquid film is firstly established, and then this model is combined with the non-dominated Sorting Genetic Algorithm-II (NSGA-II) for multi-objective optimization of the coupled multiple structural parameters with the objective of the separation efficiency and pressure-loss ratio.

2. Numerical modeling

2.1. A novel gas-liquid three-field two-phase CFD model

A novel gas-liquid three-field two-phase CFD model based on heterogeneous condensation and Euler-Lagrange-Euler solver was developed for fluid flow simulation. As shown in Fig. 3, the model includes the control equations for each of the three fields. The establishment of this model must adhere to the following premises.

(1) The inlet fluid consists of compressed gas, droplets, and water vapor.

(2) The model considers the growth of droplets. Only the heterogeneous condensation of external droplets is considered, since homogeneous condensation has a minor impact on the performance of supersonic separator (SS),

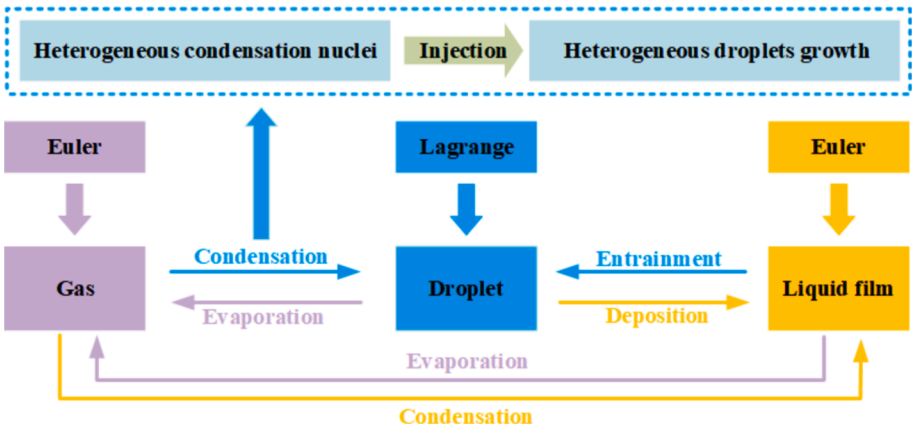

Fig. 3. Schematic diagram of the three-field two-phase model.

(3) The model considers condensation [46] and evaporation between the gas and the liquid, as well as deposition and entrainment between droplets and film.

Eqs. (1)-(4) are the mass, momentum and energy conservation equation of the gas phase, as well as the transport equation between the components of the gas phase:

$$\frac{\partial \rho_g}{\partial t} + \nabla \cdot \left(\rho_g \vec{u}_g \right) = \dot{m}_{pg} \tag{1}$$

$$\frac{\partial}{\partial t}\left(\rho_g \vec{u}_g \right) + \nabla \cdot \left(\rho_g \vec{u}_g \vec{u}_g \right) = -\nabla p + \nabla \cdot \overline{\overline{\tau}_{eff}} + \rho_g \vec{g} + U_{pg} \tag{2}$$

$$\frac{\partial (\rho_g E)}{\partial t} + \nabla \cdot \left[(\rho_g E + p) \vec{u}_g \right] = \nabla \cdot \left(\lambda_{eff} \nabla T_g + \overline{\overline{\tau}_{eff}} \cdot \vec{u}_g \right) + Q_{pg} \tag{3}$$

$$\frac{\partial \left(\rho_g \dot{Y}_i \right)}{\partial t} + \nabla \cdot \left(\rho_g \vec{u}_g \dot{Y}_i \right) = -\nabla \cdot \vec{J}_i + \dot{m}_i \tag{4}$$

Where subscripts p, f, g and i represent droplet, liquid film, gas and species.$\dot{m}_{pg}$ and $\dot{m}_{fg}$ represent mass transfer between two fields. α and ρ are volume fraction, and density.$\dot{m}_i$. is the mass source of the component i. p, u and T are pressure, velocity and temperature, respectively. U_{pg} and Q_{pg} represent momentum and energy transfer from droplets to gas. For dry gas components $\dot{m}_i = 0$, for vapor $\dot{m}_i = \dot{m}_{pg}$. E represents the energy of the gas phase. $\vec{g}$ is gravity acceleration. h_i、$\vec{J}_i$、$\dot{Y}_i$ are the specific enthalpy, diffusion flux, and mass fraction of species i, respectively. $\overline{\overline{\tau}_{eff}}$ represents the equivalent stress tensor.

The droplet trajectory equation is as follows:

$$m_p \frac{d\vec{u}_p}{dt} = m_p \left(\vec{u}_g - \vec{u}_p \right) \frac{18\mu}{\rho_p d_p^2 C_c} + m_p \frac{\vec{g}(\rho_p - \rho_g)}{\rho_p} \tag{5}$$

where m_p, d_p, μ, C_c are the droplet mass, diameter, dynamic viscosity and Cunningham correction to Stokes' drag law [47]. C_c is expressed as follows:

$$C_c = 1 + \frac{2l}{d_p}\left(1.257 + 0.4e^{-\frac{1.1 d_p}{2l}} \right) \tag{6}$$

where l is the mean free path of the droplet molecule. When the distance between the two liquid droplets is very close, a collision may occur, and the O'Rourke algorithm [48] is used to calculate the effect of collision on the droplet. The defined collision conditions are: the two liquid droplets move to the same cell, the result of the collision may be coalesced, rebound or broken.

Eqs. (7)-(9) are the mass, momentum and energy conservation equation of the liquid film.

$$\frac{\partial}{\partial t}(\rho_l \delta) + \nabla_{sur} \cdot \left(\rho_l \delta \vec{u}_f \right) = \delta \left(\dot{m}_{pf} + \dot{m}_{gf} \right) \tag{7}$$

$$\begin{aligned} &\frac{\partial}{\partial t}\left(\rho_l \delta \vec{u}_f \right) + \nabla_{sur} \cdot \left(\rho_l \delta \vec{u}_f \vec{u}_f \right) = \\ &-\delta \cdot \nabla_{sur} p_L + \rho_l \delta \vec{g}_\tau + \frac{3}{2}\vec{\tau}_{fg} - \frac{3\mu_l \vec{u}_f}{\delta} + \delta \left(\dot{m}_{pf} + \dot{m}_{gf} \right) \vec{u}_f \end{aligned} \tag{8}$$

$$\begin{aligned} &\frac{\partial}{\partial t}(\rho_l \delta h_f) + \nabla_{sur} \cdot \left(\rho_l \delta h_f \vec{u}_f \right) \\ &= \frac{\lambda_l}{\delta}(T_{sur} + T_w - 2T_m) + \delta \left(\dot{m}_{pf} + \dot{m}_{gf} \right) h_{lg} \end{aligned} \tag{9}$$

$$\dot{m}_{gf} = \frac{1}{\delta} \frac{\rho_g \dot{M} / D}{\rho_g \dot{M} / D + C_{phase}} C_{phase} \left(\dot{Y}_{sat} - \dot{Y}_v \right) \tag{10}$$

$$\dot{m}_{pf} = \dot{m}_{de} - \dot{m}_{se} - \dot{m}_{st} \tag{11}$$

Where δ is the film thickness.$\dot{M}$, ρ_g, C_{phase}, $\dot{Y}_v$ and $\dot{Y}_{sat}$ represent mass diffusivity of the water vapor, density of the gas mixture, phase change constant, vapor mass fraction and the saturation vapor mass fraction. Subscripts *sur*, *w*, *m* and *l* represent film surface, wall, film half-depth and liquid.$\dot{m}_{de}$, $\dot{m}_{se}$ and $\dot{m}_{st}$ represent the mass source contributed by droplet deposition, liquid film separation and liquid film stripping. When relative velocity between gas core and liquid film is high, the surface of film will form and grow Kelvin-Helmholtz waves. Finally, the liquid droplets will be stripped from the surface of film. D represents the distance from the center of the mesh element to the wall.

U_{gp} and $\dot{m}_{gp}$ represent momentum transfer and mass transfer from gas phase to the discrete droplets. $\dot{m}_{gp}$ and U_{gp} equation are as follows:

$$\dot{m}_{gp} = \frac{\Delta m_p}{m_{p,0}} \frac{q_{p,0}}{V_{cell}} \tag{12}$$

$$U_{gp} = \sum \left[\left(\vec{u}_g - \vec{u}_p \right) \frac{18\mu}{\rho_p d_p^2 C_c} + \frac{\vec{g}(\rho_p - \rho_g)}{\rho_p} \right] \dot{m}_{gp} \Delta t \tag{13}$$

$$\Delta m_p = \rho_p A_p \frac{dr}{dt} \Delta t \tag{14}$$

$$\frac{dr}{dt} = \frac{\sum_{i=1}^{2} a_i}{\rho_l h_{lg}} (T_r - T_v) \tag{15}$$

where Δm_p is the mass change of the droplet after passing through the control volume, and $m_{p,0}$ and $q_{p,0}$ are the initial mass and initial mass flow rate of the droplet at the inlet of the control volume.A_p is the surface area of the droplet. V_{cell} is the volume of the control volume, and Δt is time step. a_i represent the heat transfer coefficient between droplets and species i. $\frac{dr}{dt}$ represent growth rate of the droplet. T_r and T_v represent droplet surface temperature and water vapor temperature.

The Kelvin Helmholtz equation provides a formula [49] for calculating the critical radius at which droplets can nucleate:

$$r_c = \frac{2\sigma}{\rho_l R_v T_v ln(S_s)} \tag{16}$$

where r_c and σ are the critical nucleation radius and droplet surface tension, R_v is the specific gas constant of water vapor, and S_s is supersaturation.

2.2. Solution strategy

The solver type was transient pressure-based, and the solving method used implicit equation and Roe-FDS flux type. The governing equation was calculated using the second-order upwind equation. The inlet boundary is total pressure inlet. The outlet boundary condition is static pressure outlet. When droplets collide with the wall, the discrete phase boundary conditions on the wall are sedimentation, fragmentation, or rebound. When the droplets move to the dry gas outlet, the discrete phase boundary condition is considered as escape. It is necessary to introduce source terms to calculate the heat and mass exchange between three fields, as well as models for droplet nucleation and growth, and to record and update the information of heterogeneous condensation nuclei in each time step.

During the solving process, the overall computation was advanced through alternating calculations of the three-field equations until convergence was achieved. When calculating discrete liquid droplets, the solution was obtained by reading the information of externally

recorded heterogeneous condensation nuclei at each time step.

3. Experimental results

3.1. Experimental measurement systems

Fig. 4 (a) shows the experimental measurement system for the supersonic separation. A humid gas with a certain pressure, temperature, and humidity was mixed with heterogeneous droplets with a certain particle size and concentration, and then passed into the inlet of the SS for condensation experiments. Through experiments, pressure along the separator and liquid film thickness at the liquid outlet could be measured. Additionally, the dimensional parameters of the structure used in the experiment and the grid used in the simulation are shown in Fig. 4 (b).

During the design of the device, pressure measurement ports were pre-installed in the expansion section to measure the pressure during fluid flow. The measurement of droplet diameter was conducted using an extinction method device. Since the transmittance of light varies with the diameter of the droplets, the extinction method device emits and receives light, and by comparing the difference in intensity between the two, the diameter of the droplets can be calculated. The theoretical measurement range of the extinction method device used in this paper is 0.01 to 10 μm. The measurement of liquid film thickness is carried out using an FPC conductivity-based liquid film thickness measurement system. The liquid film is placed between two electrodes, and the thickness of the liquid film directly affects the current between the electrodes. By measuring the current, the thickness of the liquid film can be calculated.

When evaluating the performance of SS, it is necessary to comprehensively consider two factors: energy utilization and mass separation, and seek a balance between the two. Therefore, this article evaluates separation efficiency and pressure loss ratio from the perspectives of energy and mass.

Quality separation performance evaluation indicator:

(1) Separation efficiency η:

$$\eta = \frac{q_{\Phi,in} - q_{\Phi,out}}{q_{\Phi,in}} \times 100\% \tag{17}$$

where the subscript "Φ"represents the substances to be separated, such as CO_2, H_2O, etc., q is the mass flow rate, and its unit is kg/s.

Energy consumption performance evaluation indicator:

(2) Pressure loss ratio γ:

$$\gamma = \frac{p_{in}^* - p_{out}^*}{p_{in}^*} \tag{18}$$

where the superscript "*"represents the stagnant state, γ is a dimensionless number.

This paper uses these two parameters to evaluate the performance of supersonic separators in terms of quality separation and energy consumption. Ultimately, these two parameters are also used as objective functions for multi-objective optimization.

3.2. Experimental results

Different experimental conditions were changed to conduct multiple sets of experiments, as shown in Table 1. And p_{in}, p_{out}, T_{in}, RH_{in}, d_{in} and ρ_{in} are inlet pressure, outlet pressure, inlet temperature, inlet humidity, the diameter of inlet heterogeneous droplets and concentration of injected heterogeneous droplets, respectively. Case 1 in the table represents gas-phase experiments, and Case 2 represent liquid-phase experiments. Simulations are also conducted under these conditions using the model established in Chapter 2. The simulation results are then compared with the experimental results to verify the accuracy of the model established in Chapter 2.

Fig. 5 illustrates the pressure ratio along the wall of the SS from both the experiment and the simulation of Case 1. The results from both are highly consistent, with an R^2 value of 0.96 and an RMSE value of 0.0477. Therefore, the established model can effectively predict the gas-phase

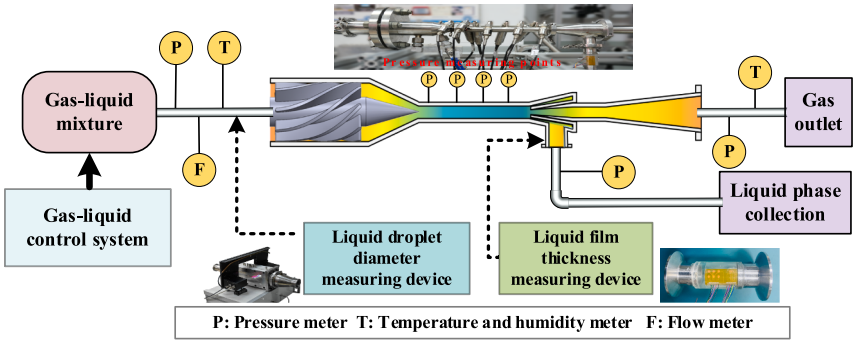

(a) Experimental measurement system for supersonic separation

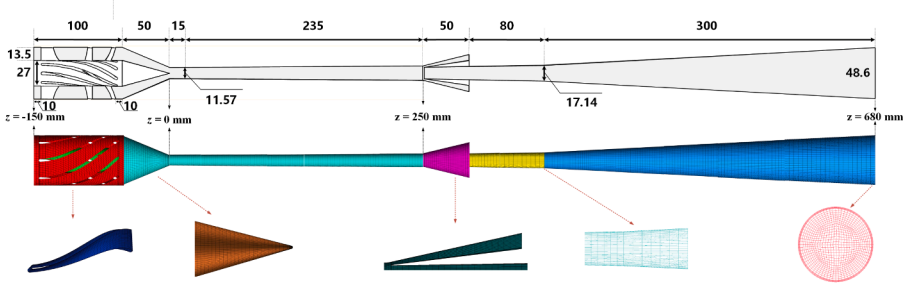

(b) Structure and three-dimensional mesh used in the simulation

Fig. 4. Experimental measurements and numerical studies for supersonic separation.

Table 1
Conditions for SS experiments.

Case	p_{in}(atm)	p_{out}(atm)	T_{in}(K)	RH_{in}(%)	d_{in}(μm)	ρ_{in}(kg/m^3)	Validation
Case 1	3	1	313	100	0	0	Gas
Case 2	3	1	300	100	2.2	0.100	Liquid

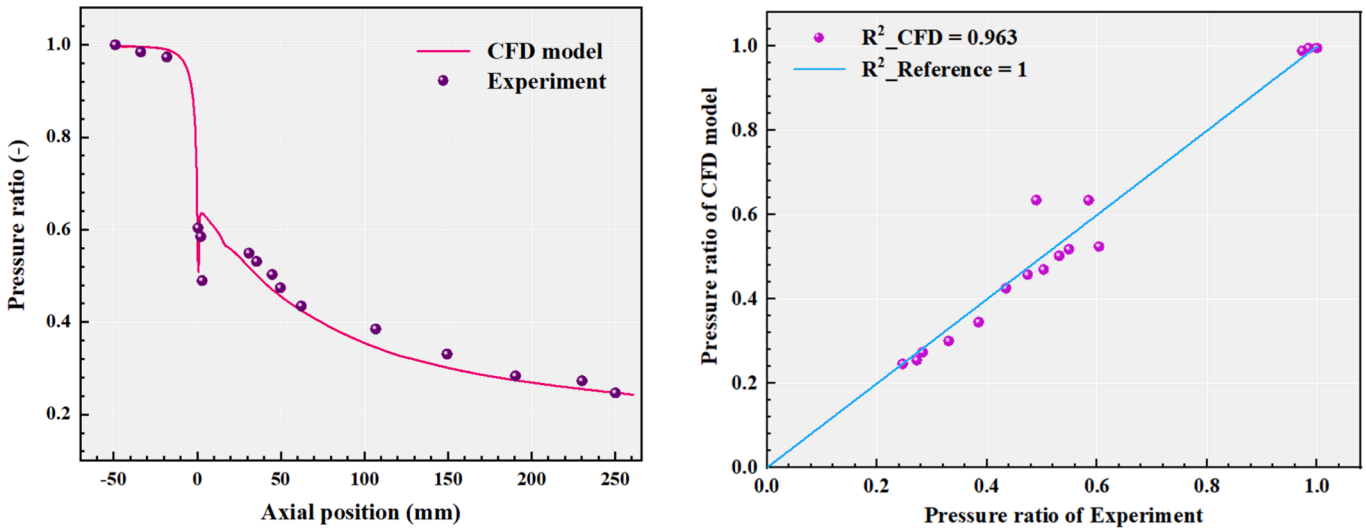

Fig. 5. Gas pressure distribution along the wall surface of the supersonic nozzle.

flow of SS.

At liquid outlet position, the liquid film thickness at liquid outlet position of Case 2 within 120 s was measured using an FPC liquid film measurement device, as shown in Fig. 6 (a). In Fig. 6 (b), the time averaged value of film thickness was compared with the simulation results. The liquid film thicknesses at the liquid outlet of Case2 obtained from this experiment was 89.239 μm, respectively. The corresponding simulation results was 88.153 μm, respectively. And the relative error between the experiment and simulation is only 1.2. It can be seen that the experimental results of both the gas phase and the liquid phase are in good agreement with the simulation results, indicating that the established model is fairly accurate.

4. Performance and optimization of supersonic separation

4.1. Two-phase flow in supersonic separator (SS)

A high-speed swirl field is generated, which can throw droplets onto the wall to achieve gas-liquid separation, in SS. In Fig. 7, contours are provided for the distribution of pressure, temperature, Mach number, and water vapor mass fraction at the axial cross-section of the SS under conditions of case 2. The line plots in the Fig. 7 depict the specific

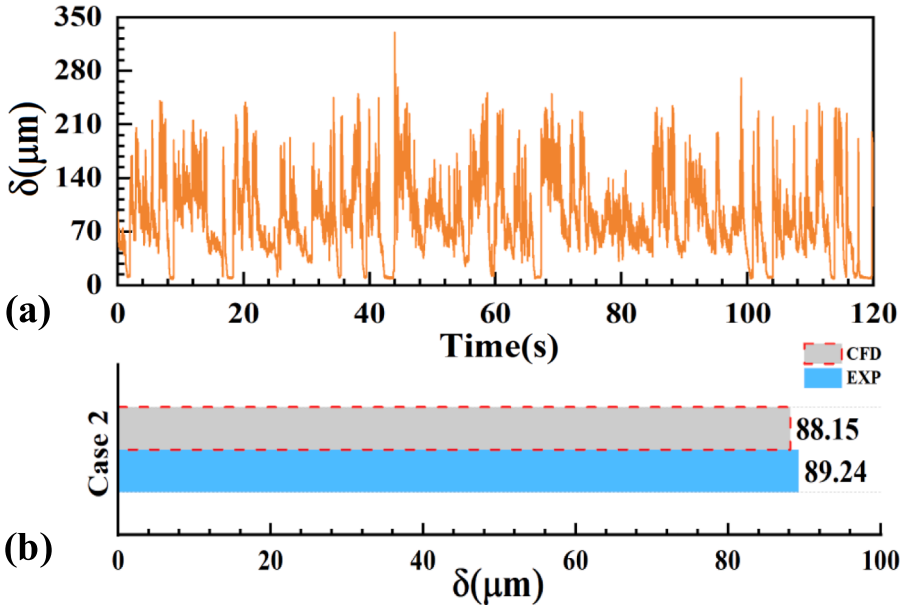

Fig. 6. Film thickness of liquid outlet obtained by experiment and CFD model.

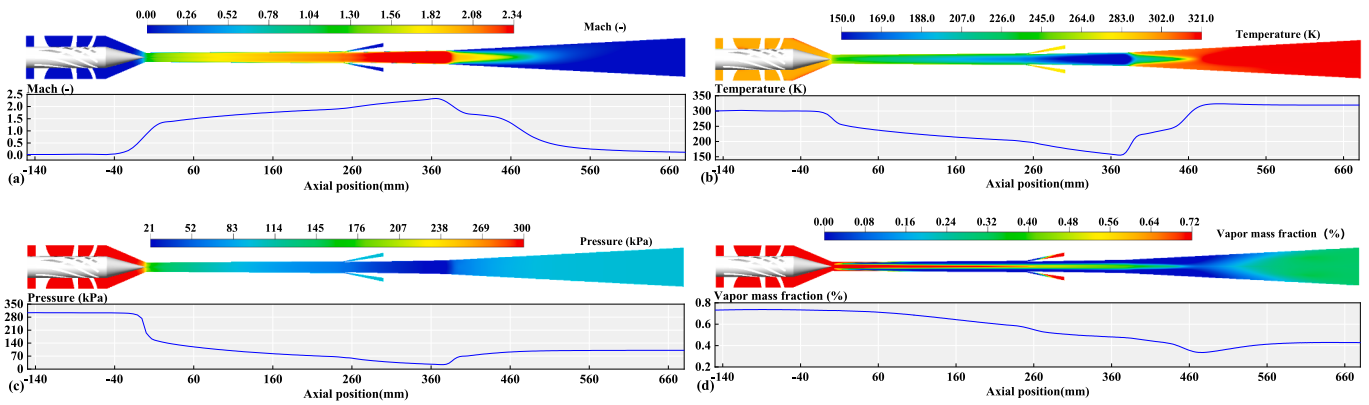

Fig. 7. Flow parameters of the fluid in SS.

distributions of Mach, temperature, pressure, and water vapor mass fraction along the axial line. As fluid enters convergent section from the static blades, the pressure and temperature gradually decrease while the velocity increases; when fluid reaches the throat of the nozzle, the velocity is essentially Mach 1; as the fluid continues to flow and enters the divergent section through the throat, the pressure and temperature decrease significantly while velocity continues to increase; until entering diffuser, where pressure and temperature recover while velocity decreases. In divergent section of SS, low temperature and pressure environment promote condensation of water vapor. Upon entering diffuser, the increase in pressure and temperature promotes evaporation. Overall, vapor mass fraction at inlet is higher than that at outlet, indicating that SS exhibits vapor separation effectiveness.

Fig. 8(a) illustrates the distribution of heterogeneous droplets and their diameters in the SS. It can be observed that in the convergent section, collisions and coalescence between droplets lead to the formation of larger droplets. Upon entering the divergent section, due to condensation, the diameter of droplets gradually increases. Then droplets were thrown onto the wall, with most of them flowing out at the liquid outlet, while a few may remain in the diffuser, with their diameters gradually decreasing. Under this condition, the droplets are not completely separated, indicating poor performance in water vapor removal. Therefore, optimization is deemed necessary. Fig. 8(b) illustrates the distribution of liquid film thickness in the SS. It can be observed that after the fluid enters the convergent section, film begins to form. Furthermore, during this flow process, thickness of liquid film continues to increase. Particularly, at the liquid outlet, there is a sharp increase in the film thickness, and liquid film is entirely discharged at liquid outlet. Fig. 8(c) shows the distribution of the liquid film temperature, where it can be seen that the overall temperature of the liquid film is greater than 273 K. As the liquid film flows from the contraction section to the diffuser section, its temperature continues to decrease, only rising again after entering the liquid discharge unit.

4.2. Geometric design and structural influence

After passing through the divergent section, the fluid directly enters the drainage device, where the liquid film flows out from the drainage device. This dehydration process is fast and relatively independent. Therefore, omitting the drainage device will generally not affect the flow field. To more accurately assess the impact of the liquid discharge device on the pressure loss ratio and separation efficiency, the liquid discharge device was removed from the original structure, resulting in a simplified configuration. A simulation of this simplified structure was conducted under the conditions described in Section 3.2. The vapor mass fraction

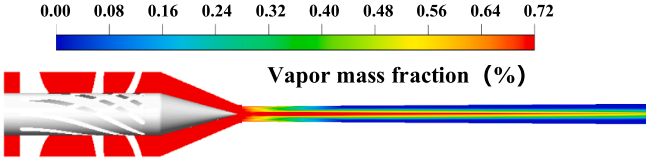

Fig. 9. Simplified structure of vapor mass fraction distribution.

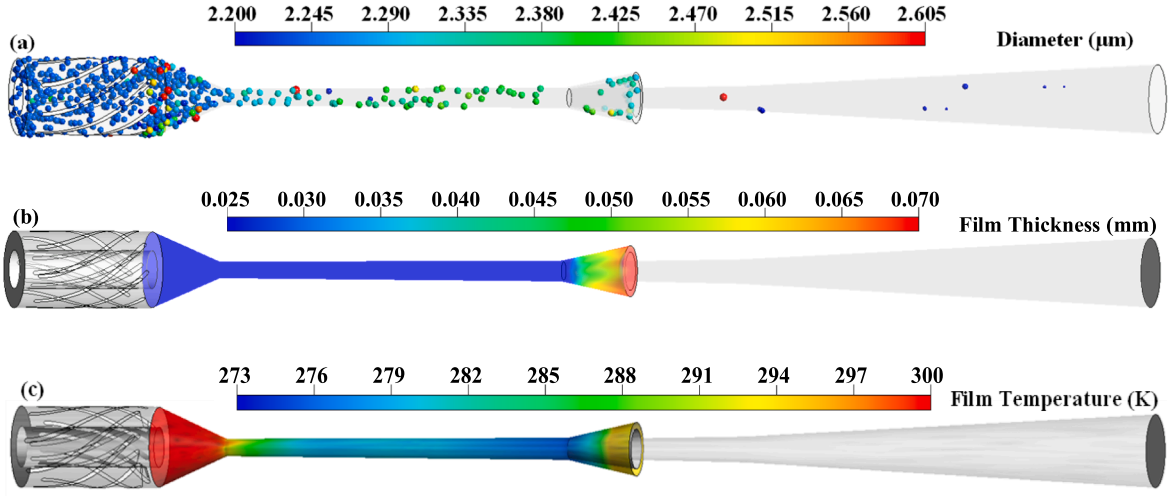

Fig. 8. The distribution of heterogeneous droplet diameters and film thickness in the SS.

contour is shown in Fig. 9, and a comparison between the simplified and original structure simulation results is shown in Fig. 10. It can be observed that omitting the liquid discharge device has virtually no effect on the flow field, pressure loss ratio, and separation efficiency. Therefore, in this paper, no optimization analysis was conducted on the drainage structure. The structure of the SS was reasonably simplified, retaining only the swirl generator and Laval nozzle sections. The simplified structure is shown in Fig. 11. The green part represents the hub, while the gray part represents the shroud of the SS, and the passage exists between them, in Fig. 11. It can be seen that there is also a hub at the throat and beyond the throat. The structure shown in Fig. 4 represents a special case where the radius of the hub at the throat is 0. The static blades of the swirl generator are also distributed between the hub and the shroud, comprising a total of 8 identical static blades. Additionally, there are 10 mm straight pipe sections before and after the static blade region.

The shape of the convergent section has an important impact on the uniformity of flow at the nozzle outlet. There are various curve algorithms for optimizing the design of axisymmetric nozzle convergent sections, such as one-dimensional flow formulas, Witozinsky curves, bicubic curves, and quintic curves. In this paper, quintic curves are chosen to design the convergent sections of the hub and shroud of the Laval nozzle, and calculation formula is as follows:

$$\frac{R-R_t}{R_{in}-R_t}=1-10\left(\frac{z}{L_1}\right)^3+15\left(\frac{z}{L_1}\right)^4-6\left(\frac{z}{L_1}\right)^5 \tag{19}$$

Where, R_{in} and R_t are the radii of the inlet and throat, R is the sectional radius of the nozzle convergent section at a certain position z, and L_1 is the length of the convergent section. The flow rate of the SS remains constant, thus flow areas at nozzle inlet and throat are set to A_{in} and A_t as 1717.67 mm^2 and 105.07 mm^2, respectively. Therefore, by changing $R_{hub,in}$, $R_{hub,t}$, and L_1, new values of $R_{shroud,in}$ and $R_{shroud,t}$ can be calculated, thereby obtaining different profiles. The divergent angle of divergent section is also a fixed value, and by changing the nozzle area expansion ratio AR (A_{out}/A_t) , different lengths of the divergent section L_2 can be obtained.

Fig. 12 shows the profile lines of the hub and shroud of SS, as well as the grid of the blades and convergent section. The green dots in Fig. 12 represent control points of the hub profile, while the blue dots represent control points of the shroud profile. The z-axis is set as the axis of rotation, with z = 0 mm representing the throat position. From left to right, the z-axis comprises areas of 10 mm straight pipe section, 80 mm static blade section, 10 mm straight pipe section, quintic curve contraction section, 15 mm straight pipe section, and divergent section. Using different profile lines, it is possible to design 1/8 of the supersonic separator with different structures in the software. Then, by periodic rotation, a complete supersonic separator can be obtained. From the grid in Fig. 12, it can be observed that grid refinement is performed at the junctions of the blades with the hub and shroud, as well as in the near-wall regions. The total number of grids is controlled between 250,000 and 300,000.

Using the aforementioned geometric design methodology, simulations were conducted for multiple cases with different structures, and the specific structural information of each case is provided in the Table 2. The specific operating conditions for simulation are: p_{in} = 3 atm, p_{out} = 1 atm, T_{in} = 300 K, RH_{in} = 100 %, $d_{het,in}$ = 8 μm, $\rho_{het,in}$ = 0.050 kg/m^3. The influence of the structure of the SS on its performance was investigated. The experimental results shown in Fig. 13 indicate that different values of L_1, $R_{hub,in}$, $R_{hub,t}$, and AR have a significant impact on the performance of SS. Therefore, it is meaningful to perform multi-objective optimization on the structure of the SS.

4.3. Multi-objective optimization method (MOOM)

In this article, MOOM was constructed by combining design of experiment, numerical simulation, surrogate model, and optimization algorithm to achieve the goal of optimizing the geometric structure of SS.

Design of experiment (DOE) is a systematic research approach aimed at exploring and understanding the relationships between different

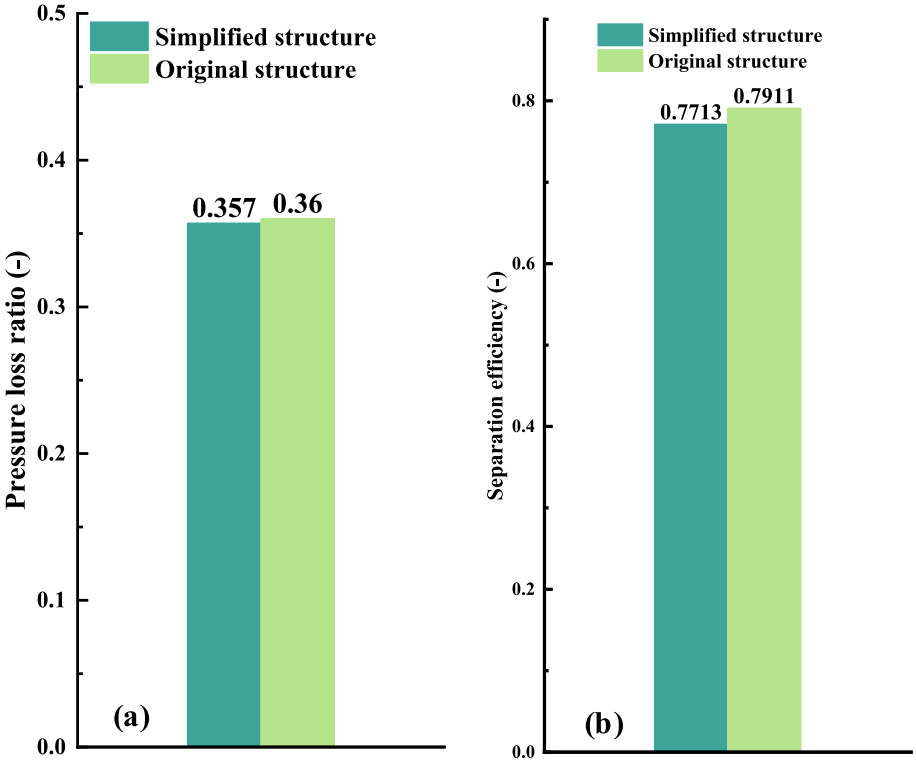

Fig. 10. Comparison of Simplified Structure and Original Structure Simulation Results.

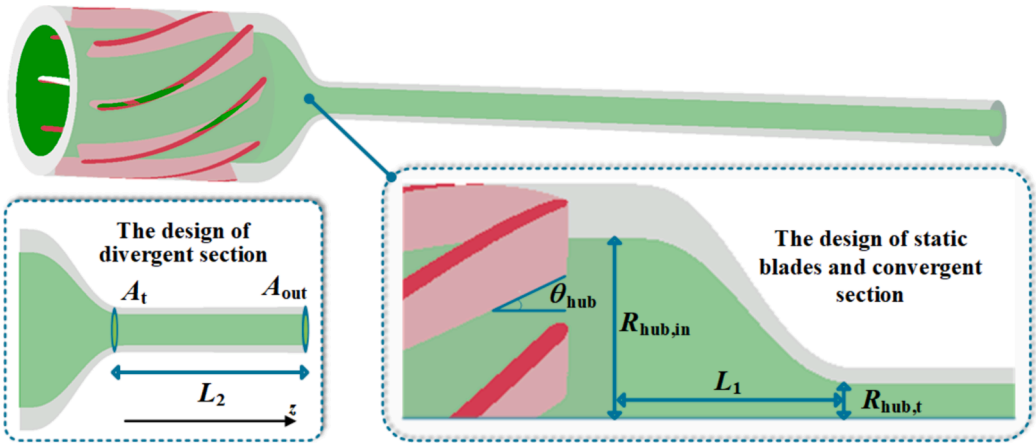

Fig. 11. The geometric design of the SS.

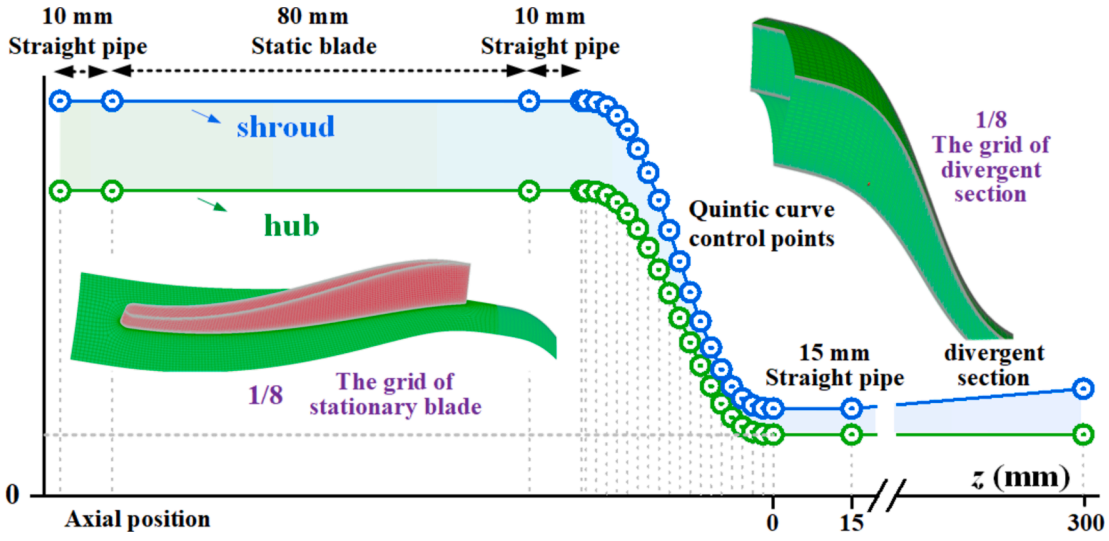

Fig. 12. The profile lines and grid of the SS.

Table 2
Conditions for simulations.

Case	X_1	X_2	X_3	X_4
Case 3	20	27.5	6.75	1.1
Case 4	50	27.5	6.75	1.1
Case 5	100	27.5	6.75	1.1
Case 6	60	15	6.75	1.3
Case 7	60	30	6.75	1.3
Case 8	60	45	6.75	1.3
Case 9	60	27.5	0.5	1.2
Case 10	60	27.5	7.5	1.2
Case 11	60	27.5	13.5	1.2
Case 12	60	15	6.75	1.1
Case 13	60	15	6.75	1.6

variables through effectively organizing experiments [50]. The core objective of DOE is to obtain the maximum information with the minimum number of experiments, thereby gaining a more comprehensive understanding of the relationships between optimizing variables and objective functions. In this paper, Optimal Latin Hypercube Sampling (OLHS) was chosen for DOE [51]. OLHS is an effective sampling method that ensures sufficient regularity in the selected sample space for model construction.

Surrogate model refers to the method of using a simplified model to approximate complex phenomena or system behaviors in practical problems [52]. In many cases, complex phenomena are difficult to model or analyze directly, and surrogate models can reduce the complexity of the problem while maintaining reasonable accuracy. Surrogate model is a key point in MOOM because it can greatly influence the final optimization results. And Response Surface Model (RSM) was chosen to construct surrogate model [53].

After establishing the surrogate model, appropriate optimization algorithm can be used for optimization. And optimization algorithm used was the Non-dominated Sorting Genetic Algorithm-II (NSGA-II). Genetic Algorithm (GA) is an optimization algorithm that simulates natural selection and genetic mechanisms. It gradually optimizes the solution space through iterative evolution. Its performance is very powerful [54]. The NSGA-II used in this paper is an improvement over traditional genetic algorithm [55]. It adopts the basic framework of GA and introduces employing fast non-dominated sorting method, crowding distance sorting method, and elitist strategy.

The specific flowchart of NSGA-II is shown in Fig. 14. Firstly, a moderately sized initial population is randomly generated, and then the initial population is obtained through selection, crossover, and mutation operations. Subsequently, the initial population is subjected to non-dominated sorting and crowding distance calculation to ensure that individuals in the population obtain appropriate sorting and density distribution on the Pareto front. As the genetic generation progresses,

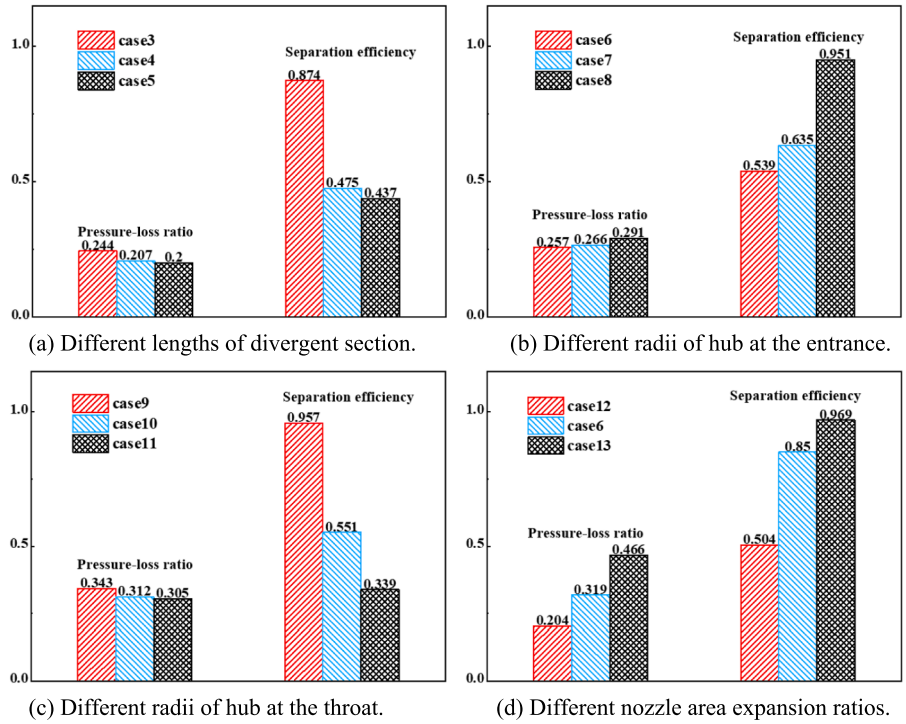

(a) Different lengths of divergent section. (b) Different radii of hub at the entrance.

(c) Different radii of hub at the throat. (d) Different nozzle area expansion ratios.

Fig. 13. The influence of different design variables on the objective function.

parents and offspring are selectively merged based on the results of nondominated sorting and crowding distance calculation. New offspring are generated through crossover and mutation operations, and then subjected to nondominated sorting and crowding distance calculation. This iterative process is repeated until the preset genetic generation is reached, and then the computation is terminated. Through this process, the Pareto front can be efficiently searched.

In multi-objective optimization problems, there typically exist conflicting relationships among objective functions. There is no single solution that can optimize all objectives simultaneously. The mathematical model is shown as follows:

$$\min OF(x) = [OF_1(X), OF_2(X), \cdots, OF_n(X)]^T \tag{20}$$

$$s.t. \begin{cases} G_i(X) \le 0, i = 1, \cdots, p \\ H_j(X) = 0, j = 1, \cdots, q \\ lower_k \le X_k \le upper_k, k = 1, \cdots, n \end{cases} \tag{21}$$

where $G_i(X) \le 0$ represents inequality constraints, $H_j(X) = 0$ represents equality constraints, and $lower_k \le X_k \le upper_k$ denote the lower and upper bounds of design variables. In this paper, objective function OF is set as pressure loss ratio γ and separation efficiency η, and L_1, $R_{hub,in}$, $R_{hub,t}$, and AR are selected as design variables. Table 3 shows multi-objective optimization problem of geometric structure of SS in this paper. The range of design variables has been rigorously derived. Exceeding this range would generally lead to either excessive sacrifice of separation efficiency to optimize pressure loss ratio or vice versa, both of which are unacceptable. The overall optimization process is depicted in Fig. 15.

The OLHS method was used to uniformly select 174 sets of sample points in the sample space. The geometric design method introduced in Section 3.1 was used to design the corresponding geometries for the 174 sets of sample points, obtaining 174 corresponding geometric structures and grids. The established gas–liquid model was used to perform CFD calculations for all samples, obtaining the objective function values OF_1 and OF_2. The CFD simulation was conducted with the inlet and outlet conditions set as $d_{in} = 8$ μm, $p_{in} = 3$ atm, $p_{out} = 1$ atm, $T_{in} = 300$ K, $T_{out} = 100$ K, $\rho_{in} = 0.050$ kg/m^3. The results are shown in Fig. 16, indicating that pressure loss ratio OF_1 is distributed between 0–52%, and the separation efficiency OF_2 is distributed between 0–100%.

The 174 sets of samples were divided into a training set and a validation set. The training set contains 164 sets of samples, used to fit the Response Surface Model (RSM), while the validation set contains 10 sets of samples, used to test the accuracy of RSM. Specific values of the RSM coefficients for OF_1 and OF_2 were present in Table 4, where terms with insignificant effects on the response variables have been eliminated. Therefore, the final determined second-order RSM is defined as follows:

$$\begin{aligned} OF_1 = & -1.100 - 0.013X_3 + 1.754X_4 + 5.448 \\ & \times 10^{-5}X_2^2 + 0.0003X_3^2 - 0.474X_4^2 - 5.311 \\ & \times 10^{-5}X_1X_2 + 0.0001X_1X_3 \end{aligned} \tag{22}$$

$$\begin{aligned} OF_2 = & -1.824 - 0.017X_1 + 4.119X_4 + 0.0001X_1^2 + 0.0001X_2^2 \\ & - 1.443X_4^2 - 0.0006X_1X_3 + 0.005X_1X_4 \end{aligned} \tag{23}$$

In the process of constructing the RSM, the parameters with smaller effects, i.e., those with smaller coefficients, were omitted. For quantitative evaluation of the accuracy of the established RSM, root mean square error ($RMSE$), the average relative error (ARE), and R^2 are used to evaluate the performance of RSM, calculated as follows:

$$\begin{cases} R^2 = 1 - \dfrac{\sum_{i=1}^{num}\left(\widehat{y}_{i,Exp} - \widehat{y}_{i,CFD}\right)^2}{\sum_{i=1}^{num}\left(\widehat{y}_{i,Exp} - \overline{y}_{i,Exp}\right)^2} \\ RMSE = \sqrt{\dfrac{1}{num}\sum_{i=1}^{num}\left(\widehat{y}_{i,Exp} - \widehat{y}_{i,CFD}\right)^2} \\ ARE = \dfrac{\sum_{i=1}^{num}\left|\dfrac{\widehat{y}_{i,CFD} - \widehat{y}_{i,PRE}}{\widehat{y}_{i,CFD}}\right|}{num} \end{cases} \tag{24}$$

where the subscript "PRE" represents the predicted value of the RSM, and the subscript "CFD" represents the simulated value. The closer R^2 is

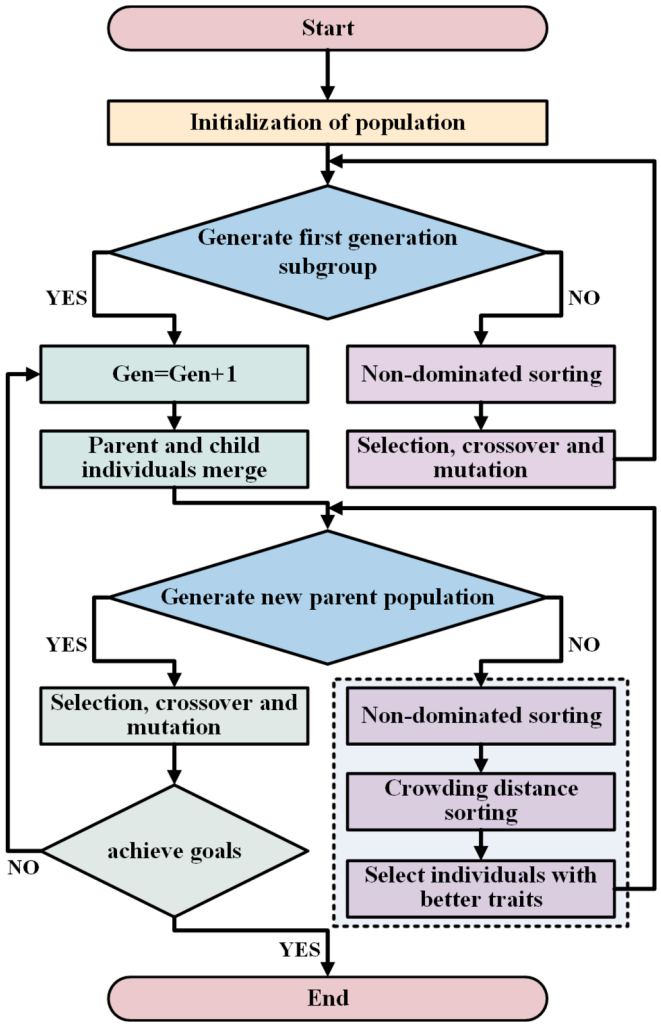

Fig. 14. The flowchart of NSGA-II.

Table 3
Objective functions and Design variables of multi-objective optimization.

	OF/X	Description	Constraint condition
Objective functions(min)	OF_1	Minimize pressure-loss ratio (γ)	$0 < OF_1 < 1$
	$-OF_2$	Maximize separation efficiency (η)	$0 < OF_2 < 1$
Design variables	X_1	The length of convergent section: L_1 (mm)	$20 \le X_1 \le 100$
	X_2	The radius of hub at the inlet:$R_{hub,in}$(mm)	$10 \le X_2 \le 45$
	X_3	The radius of hub at the throat:$R_{hub,t}$ (mm)	$0 \le X_3 \le 13.5$
	X_4	The nozzle area expansion ratio:AR (−)	$1 \le X_4 \le 1.6$

to 1, and the closer RMSE and ARE are to 0, the better the prediction performance of RSM. Table 5 presents the accuracy evaluation results of the RSM for two independent objective functions. It can be seen that for ARE and RMSE, both objective values are less than 0.12, and for R^2, both objective values are greater than 0.9. Therefore, it is considered that the prediction of OF_1 and OF_2 is reliable.

Subsequently, the constructed RSM was optimized. In Fig. 17, the blue points represent all feasible solutions obtained from multi-objective optimization, the red points represent infeasible solutions, and the green points represent the Pareto front. It can be seen that the obtained multi-objective optimization results are consistent with the classic multi-objective optimization results [56,57], showing a "C" shape. And it can be observed from all feasible solutions that when OF_1 increases,OF_2 also increases; conversely, when OF_2 decreases,OF_1 also decreases. The NSGA-II algorithm accurately identified the boundaries of OF_1 and OF_2, computing 778 non-dominated solutions for the two objective functions. This clearly demonstrates the trade-off relationship between the pressure loss ratio and separation efficiency, where lower pressure loss ratio always corresponds to lower separation efficiency. There is no clear superiority or inferiority among these solutions. In the design of supersonic separator (SS), appropriate compromises need to be made based on practical considerations.

To verify the feasibility and effectiveness of the Pareto solution set, this paper selected 4 sets of solutions from Pareto front set for numerical simulation analysis. The distribution of verification points A, B, C, D in the Pareto solution set is shown in Fig. 18(a), and the design variable parameters and objective function values corresponding to each point are shown in Table 6. As shown in Table 6, the pressure loss ratios of the optimized structures A, B, C, and D, obtained through multi-objective optimization, are 9.2%, 9.7%, 14.0%, and 23.9%, respectively, while their separation efficiencies are 53.3%, 65.1%, 80.1%, and 99.9%, respectively. New structures were designed according to the geometric structure design method proposed in 3.2, and CFD simulations were conducted under the same operating conditions. The pressure loss ratios of the optimized structures A, B, C, and D, obtained through CFD simulation, are 9.4%, 10.2%, 13.9%, and 22.9%, respectively, while their separation efficiencies are 56.1%, 65.8%, 75.8%, and 96.3%, respectively. The comparison can be seen in Fig. 18. It can be seen that simulation results of 4 sets of Pareto optimal solutions are highly consistent with prediction results of RSM. After calculation, the maximum relative error between simulated and predicted values in calculating pressure loss ratio is 5.4%, and in calculating separation efficiency is 5.3%. This demonstrates the accuracy and feasibility of the multi-objective optimization method proposed in this paper.

The structure shown in Fig. 4 is taken as the original structure and compared with the optimized structures. *AR* of each of the four optimized structures A, B, C, D is statistically calculated, and pressure loss ratio and separation efficiency of original structure at these area expansion ratios are compared with the performance of the optimized structures. As shown in Fig. 19, the pressure loss ratios of the original structure at different AR values are 11.5%, 11.5%, 19.5%, and 26.6%, respectively, while the separation efficiencies are 41.9%, 41.9%, 44.6%, and 89.3%, respectively. Compared to the original structure, the optimized structures all achieved smaller pressure loss ratio and larger separation efficiency. We also added a comparison under the same separation efficiency. With structures achieving 90% separation efficiency, the pressure loss ratio of the optimized structure was reduced by maximum 28.3%, compared to the original structure. This indicates that we achieved successful optimization results. Our optimization process is rigorous, and the results are reliable, identifying the optimal structure for separation efficiency under different pressure loss ratios. Overall, the optimization framework proposed in this paper can find new separation structures with better performance, achieving a larger mass separation while minimizing energy loss. It can be observed that the increase in separation efficiency varies across different structures, indicating that different structures are suitable for different operating ranges. The original structure is not suitable for separation under the current pressure loss ratio conditions.

Fig. 20 shows the parameter fields and droplet distribution diagrams for optimized structures B and D. Comparing these to the original structure's parameter distribution, it can be observed that under relatively low pressure loss ratios, the droplets are almost fully separated in both optimized structures. Additionally, the mass fraction of water vapor in optimized structure D is significantly lower than that of the original structure. Compared to the original structure, the reductions in pressure and temperature, as well as the increase in velocity, are smaller

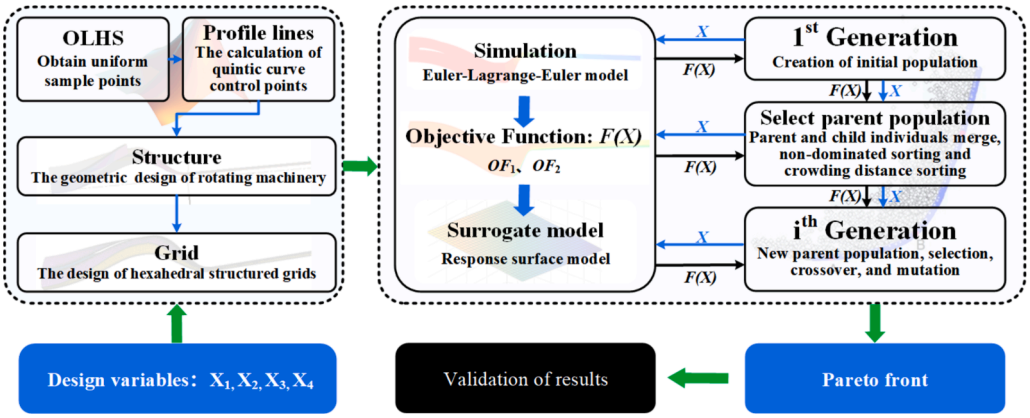

Fig. 15. The overall structure diagram of multi-objective optimization.

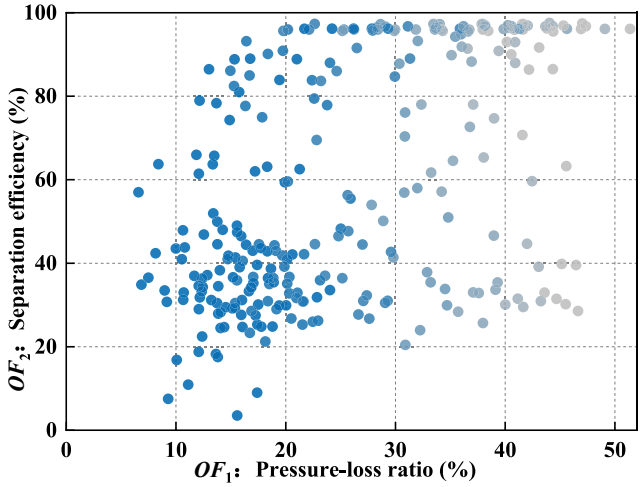

Fig. 16. Distribution of simulation results for sample individuals.

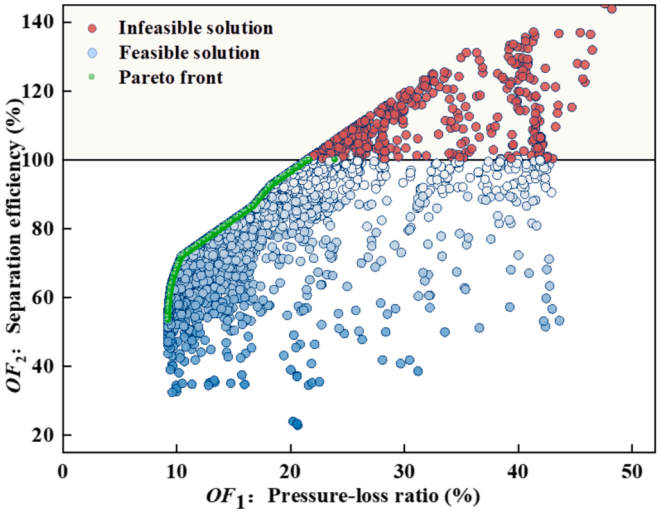

Fig. 17. Solution set for multi-objective optimization and pareto front.

Table 4
Response surface model coefficients.

OF	β_0	β_1	β_3	β_4	β_{11}	β_{22}
1	−1.100	0	−0.013	1.754	0	5.448×10^{-5}
2	−1.824	−0.017	0	4.119	0.0001	0.0001
OF	β_{33}	β_{44}	β_{12}	β_{13}	β_{14}	
1	0.0003	−0.474	-5.311×10^{-5}	0.0001	0	
2	0	−1.443	0	−0.0006	0.005	

Table 5
Evaluation of the accuracy of the response surface for two independent objective functions.

OF	ARE	RMSE	R^2
1	0.055	0.069	0.954
2	0.092	0.113	0.932

in both optimized structures. Overall, it is evident that the optimized structures have superior pressure loss ratios and separation efficiency compared to the original structure.

Comparing the two optimized structures, it can be observed that both have similar droplet separation capabilities. However, optimized structure D demonstrates better separation of water vapor, though it also has a higher pressure loss ratio. This indicates that the design concepts of

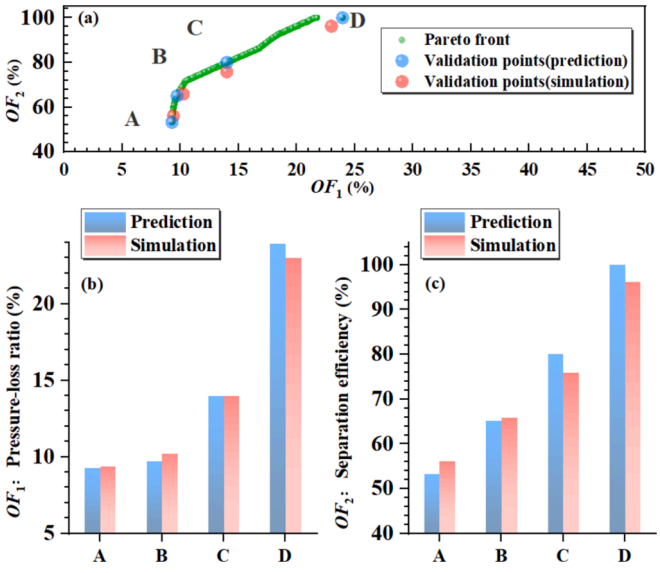

Fig. 18. Comparison between Pareto solution set and simulation.

Table 6
Cases used for validation in pareto front.

	X_1	X_2	X_3	X_4	OF_1	OF_2
A	74.7865451	44.999193	2.902216724	1.0000	0.092677184	0.533308081
B	89.6968018	44.98112465	0	1.0000	0.097081151	0.651145385
C	99.99950456	44.99572523	0.000116076	1.0907	0.139952171	0.800634602
D	20.43328289	39.50843913	0.680963205	1.2508	0.239444043	0.99995697

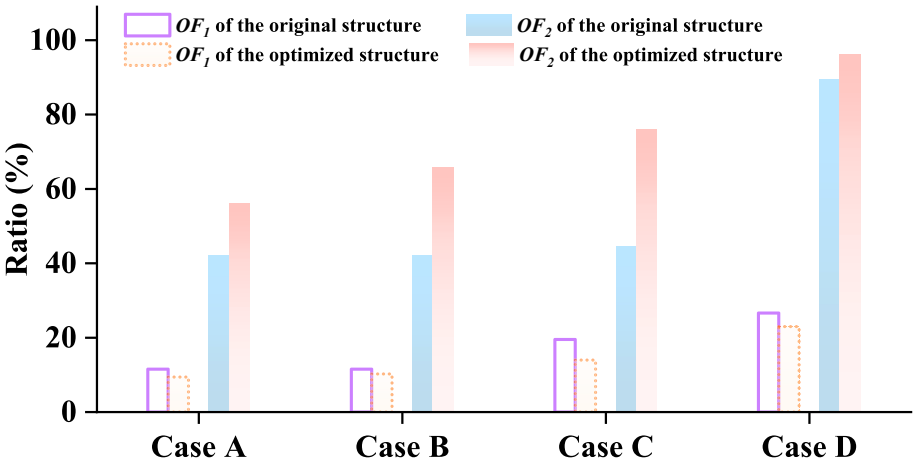

Fig. 19. Comparison between original model and optimized model.

the two optimized structures are different. Optimized structure B reduces the length of the divergent section, ensuring that its pressure loss ratio does not become too large. On this basis, it separates the majority of the droplets and a small portion of the water vapor, achieving a good separation effect. Optimized structure B provides valuable insights into the traditional design approach of sacrificing the pressure loss ratio to enhance separation efficiency. Optimized structure D retains a longer divergent section, which increases the pressure loss ratio to some extent while significantly improving the water vapor separation ability, resulting in overall higher separation efficiency. Based on the characteristics of optimized structures B and D, they are respectively suitable to serve as the first-stage supersonic separator and the second-stage supersonic separator in a two-stage dehydration process.

4.4. Cost analysis

The cost of dehydration using the triethylene glycol (TEG) process increases significantly with the amount of water processed. Combining the SS and TEG dehydration processes can significantly reduce costs. This section conducts a cost analysis based on the TEG dehydration process proposed by Neagu et al [58].

The untreated natural gas is first directed to SS and, after treatment, then directed to the TEG. This completes the design of a new dehydration process (SS + TEG). Previously, Wang et al. [59] conducted a cost analysis by combining the SS with TEG. This paper uses Wang et al.'s results as the baseline for the original SS + TEG configuration, comparing them with the optimized results. The dehydration unit composed of the optimized SS achieves a separation efficiency of 96%, which can significantly reduce the raw material costs for TEG. However, the increased complexity of the system inevitably leads to higher fixed production costs.

The total cost of production (TCOP) is calculated using equation:

$$TCOP = VCOP + FCOP + ACC \tag{25}$$

where variable cost of production (VCOP), fixed cost of production (FCOP), and annual capital cost (ACC) are determined using the same method outlined by Neagu et al. Among them, The VCOP consists of the annual TEG cost, annual steam cost, annual electrical energy cost, and annual miscellaneous cost (consumable materials, waste water treatments, waste disposal). The specific values are shown in Table 7.

It can be observed that, due to the improved separation efficiency, the optimized SS + TEG reduces the annual TCOP by $125,194 compared to the original SS + TEG and by $459,747 compared to TEG. Clearly, combining SS dehydration with TEG can significantly reduce costs, and the optimized structure selected through multi-objective optimization can further reduce costs. This is a highly effective approach.

5. Conclusions

This paper integrated design of experiment, numerical computation, Response Surface Model (RSM), and NSGA-II algorithm to construct a multi-objective optimization method. Pressure loss ratio and separation efficiency of the SS were taken as the optimization objectives, with the geometric parameters including the convergent length of the nozzle, the radius of hub at the inlet, the radius of hub at the throat, and the nozzle area expansion ratio as the design variables. Firstly, the OLHS was used for experimental design, and then structure and grid design were conducted. Subsequently, based on the established gas–liquid model, CFD simulations were performed, and simulation results were used to establish RSM. Then, NSGA-II was applied for multi-objective optimization to obtain Pareto solution set. Additionally, the reliability of results was verified using numerical simulation methods, and the performance differences between the optimized structure and the original structure were compared. The specific conclusions are as follows:

(1) It conducted simulations based on the gas–liquid three-field two-phase CFD model. And accuracy of this model is satisfactory, and it can effectively simulate the two-phase flow in the SS.

(2) Through simulation and analysis, it is determined that structural changes in the SS significantly affect its performance. Therefore, it is necessary to conduct multi-objective optimization to improve performance.

(3) A total of 174 sets of samples are used to fit the RSM. ARE and RMSE of the model's predictions for the pressure loss ratio and

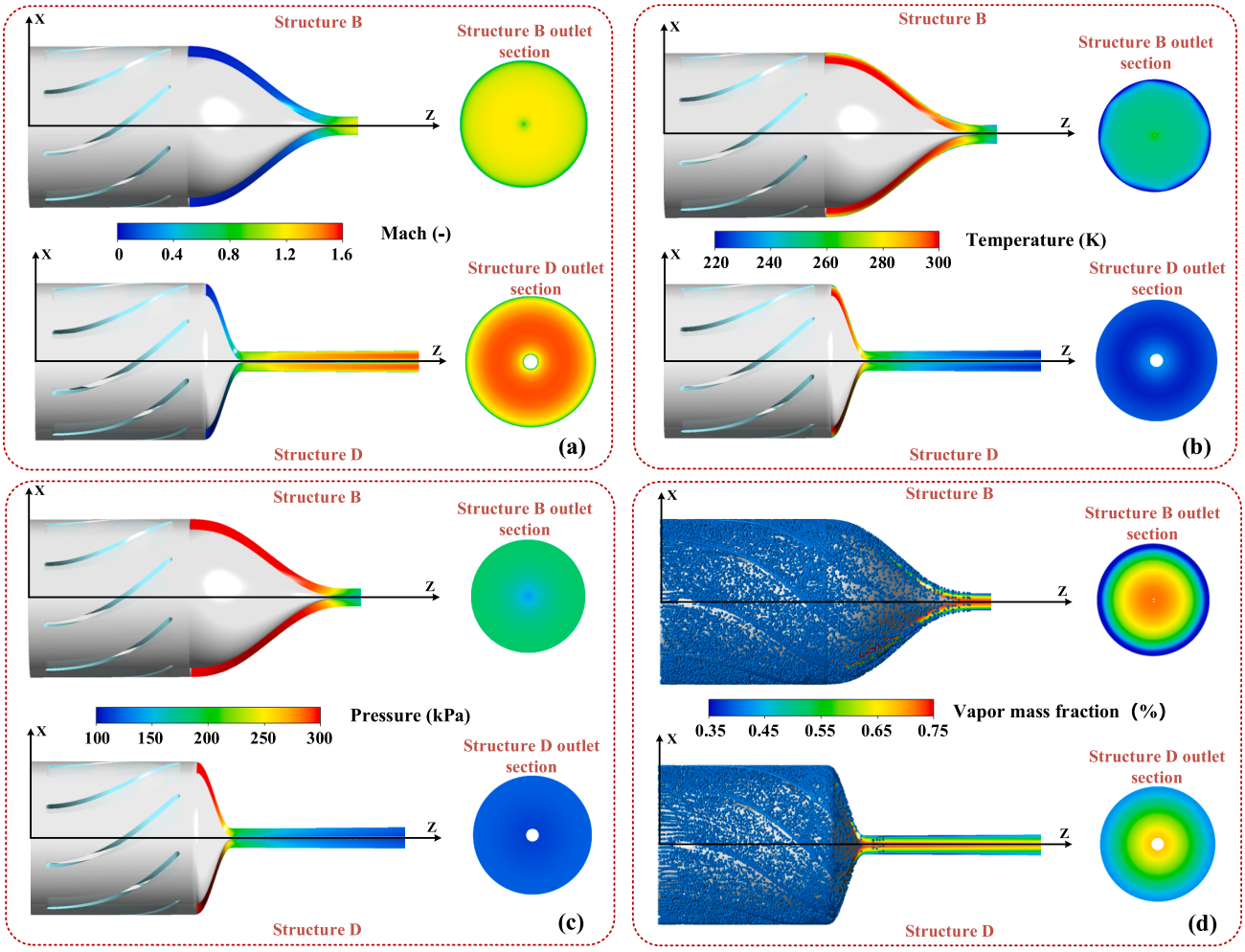

Fig. 20. The parameter distributions and droplet distribution diagrams for structures B and D.

Table 7
The cost comparison between the three processes.

Items	Optimized SS + TEG ($)	Original SS + TEG ($)	TEG ($)
Variable Cost of Production (VCOP)	817,529	818,007	843,933
Annual TEG cost	349	1,592	8,726
Annual Steam cost	751	3,426	18,778
Annual Electrical energy cost	800,000	800,000	800,000
Annual Miscellaneous cost	16,429	16,429	16,429
Annual Capital Cost (ACC)	41,339	81,409	393,476
Fixed Cost of Production (FCOP)	1,904,115	1,985,292	1,985,292
Total Cost of Production (TCOP)	2,762,954	2,888,148	3,222,701

separation efficiency are both less than 0.12, and R2 values are all greater than 0.9. It is considered that RSM is reliable for predicting the pressure loss ratio and separation efficiency.

(4) A total of 778 non-dominated solutions for the two objective functions are calculated. Numerical simulations are conducted for four sets of Pareto optimal solutions. After calculation, the maximum relative errors between simulated and predicted values for calculating pressure loss ratio and separation efficiency are 5.4% and 5.3%, respectively, demonstrating the reliability of the optimization results.

(5) The new separation structure exhibits better performance than the original structure. At the same 90% separation efficiency, the pressure loss ratio of the optimized structure was reduced by up to 28.3% compared to the original structure. This demonstrates that the optimization algorithm maximized mass separation while minimizing energy loss. Additionally, structures suitable for primary and secondary separation in the natural gas dehydration process were identified from the Pareto solutions.

CRediT authorship contribution statement

Hongbing Ding: Conceptualization, Formal analysis, Supervision, Writing – original draft, Writing – review & editing. **Guangchen Zhang:** Formal analysis, Investigation, Writing – review & editing. **Shiwei Wang:** Formal analysis, Investigation, Writing – review & editing. **Yu Zhang:** Formal analysis, Writing – review & editing. **Yan Yang:** Supervision, Formal analysis, Methodology, Writing – review & editing. **Chuang Wen:** Supervision, Formal analysis, Methodology, Writing – review & editing.

Declaration of competing interest

The authors declare that they have no known competing financial interests or personal relationships that could have appeared to influence the work reported in this paper.

Acknowledgment

This work is supported in part by the National Natural Science

Foundation of China under Grants 52276159, 51876143, and the Anhui Provincial Scientific Research Plan Program [grant number 2023AH051556].

Data availability

Data will be made available on request.

References

[1] J.K. Mwangi, W. Lee, Y. Chang, C. Chen, L. Wang, An overview: Energy saving and pollution reduction by using green fuel blends in diesel engines, Appl. Energy 159 (2015) 214–236.
[2] K.M. Chan, P. Balvanera, K. Benessaiah, M. Chapman, S. Díaz, E. Gómez-Baggethun, et al., Why protect nature? Rethinking values and the environment, Proc. Natl. Acad. Sci. 113 (2016) 1462–1465.
[3] K. Srirangan, L. Akawi, M. Moo-Young, C.P. Chou, Towards sustainable production of clean energy carriers from biomass resources, Appl. Energy 100 (2012) 172–186.
[4] J. Szoplik, Improving the natural gas transporting based on the steady state simulation results, Energy (Oxf.) 109 (2016) 105–116.
[5] G. Xu, C. Xu, M. Wang, J. Cai, Z. Chen, X. Li, Influence of nickel foam on kinetics and separation efficiency of hydrate-based Carbon dioxide separation, Energy (Oxf.) 231 (2021) 120826.
[6] J. Bian, X. Cao, W. Yang, X. Song, C. Xiang, S. Gao, Condensation characteristics of natural gas in the supersonic liquefaction process, Energy (Oxf.) 168 (2019) 99–110.
[7] A.K. Maayta, N. Al-Rawashdeh, Inhibition of acidic corrosion of pure aluminum by some organic compounds, Corros. Sci. 46 (2004) 1129–1140.
[8] A. Sakheta, U. Zahid, Process simulation of dehydration unit for the comparative analysis of natural gas processing and carbon capture application, Chem. Eng. Res. Des. 137 (2018) 75–88.
[9] M. Davis, A. Okunlola, G. Di Lullo, T. Giwa, A. Kumar, Greenhouse gas reduction potential and cost-effectiveness of economy-wide hydrogen-natural gas blending for energy end uses, Renew. Sustain. Energy Rev. 171 (2023) 112962.
[10] W. Shan, H. Chen, Y. Yuan, Y. Ma, Effectiveness of excess gas method for the preparation of hydrate-bearing sediments: Influence and mechanism of moisture content, J. Clean. Prod. 366 (2022) 132889.
[11] H. Lin, S.M. Thompson, A. Serbanescu-Martin, J.G. Wijmans, K.D. Amo, K. A. Lokhandwala, et al., Dehydration of natural gas using membranes. Part I: Composite membranes, J. Membr. Sci. 413 (2012) 70–81.
[12] Z.Y. Kong, A. Mahmoud, S. Liu, J. Sunarso, A parametric study of different recycling configurations for the natural gas dehydration process via absorption using triethylene glycol, Process Integr. Optim. Sustain. 2 (2018) 447–460.
[13] Law LC, Yusoff Azudin N, Abd. Shukor SR. Optimization and economic analysis of amine-based acid gas capture unit using monoethanolamine/methyl diethanolamine. Clean Technol Environ Policy 2018;20:451-461.
[14] S.H. Park, S.J. Lee, J.W. Lee, S.N. Chun, J.B. Lee, The quantitative evaluation of two-stage pre-combustion CO2 capture processes using the physical solvents with various design parameters, Energy (Oxf.) 81 (2015) 47–55.
[15] J.R. McDonough, R. Law, D.A. Reay, V. Zivkovic, Intensified carbon capture using adsorption: Heat transfer challenges and potential solutions, Therm. Sci. Eng. Prog. 8 (2018) 17–30.
[16] J.L. de Medeiros, A.L. de Oliveira, A.M. Teixeira, O.D.Q.F. Araújo, Offshore processing of CO2-rich natural gas with supersonic separator, Springer (2019).
[17] Brigagão GV, de Oliveira Arinelli L, de Medeiros JL, Ofélia De Queiroz FA. Low-pressure supersonic separator with finishing adsorption: higher exergy efficiency in air pre-purification for cryogenic fractionation. Sep Purif Technol 2020;248: 116969.
[18] Interlenghi SF, de Medeiros JL, Ofélia De Queiroz FA. Novel air dehydration for life-support systems of manned-spacecraft: Supersonic separator technology. Appl Therm Eng 2022;213:118731.
[19] A.M. Teixeira, A.L. de Oliveira, J.L. de Medeiros, Ofélia De Queiroz FA. Recovery of thermodynamic hydrate inhibitors methanol, ethanol and MEG with supersonic separators in offshore natural gas processing, J. Nat. Gas Sci. Eng. 52 (2018) 166–186.
[20] J. Bian, X. Cao, Supersonic separation technology for natural gas dehydration in liquefied natural gas plants, Elsevier (2024) 163–190.
[21] X. Cao, W. Yang, The dehydration performance evaluation of a new supersonic swirling separator, J. Nat. Gas Sci. Eng. 27 (2015) 1667–1676.
[22] A.L. de Oliveira, J.L. de Medeiros, D.C. de Melo, A.M. Teixeira, G.V. Brigagão, F. M. Passarelli, et al., Carbon capture and high-capacity supercritical fluid processing with supersonic separator: Natural gas with ultra-high CO2 content, J. Nat. Gas Sci. Eng. 66 (2019) 265–283.
[23] de Oliveira Arinelli L, Brigagão GV, Wiesberg IL, Teixeira AM, de Medeiros JL, Ofélia De Queiroz FA. Carbon-dioxide-to-methanol intensification with supersonic separators: extra-carbonated natural gas purification via carbon capture and utilization. Renewable and Sustainable Energy Reviews 2022;161:112424.
[24] Wiesberg IL, de Oliveira Arinelli L, Ofélia De Queiroz FA, de Medeiros JL. Upgrading exergy utilization and sustainability via supersonic separators: Offshore processing of carbonated natural gas. J Clean Prod 2021;310:127524.
[25] A.M. Teixeira, A.L. de Oliveira, J.L. de Medeiros, Ofélia De Queiroz FA. Sustainable offshore natural gas processing with thermodynamic gas-hydrate inhibitor reclamation: Supersonic separation affords carbon capture, Chem. Eng. Res. Des. 181 (2022) 55–73.
[26] E. Lakzian, S. Yazdani, F. Salmani, O. Mahian, H.D. Kim, M. Ghalambaz, et al., Supersonic separation towards sustainable gas removal and carbon capture, Prog. Energy Combust. Sci. 103 (2024) 101158.
[27] G.V. Brigagão, A.L. de Oliveira, J.L. de Medeiros, F.A. Ofélia De Queiroz, A new concept of air pre-purification unit for cryogenic separation: Low-pressure supersonic separator coupled to finishing adsorption, Sep. Purif. Technol. 215 (2019) 173–189.
[28] S.R. Shooshtari, A. Shahsavand, Numerical investigation of water droplets trajectories during natural gas dehydration inside supersonic separator, J. Nat. Gas Sci. Eng. 54 (2018) 131–142.
[29] X. Zeng, G. Fan, J. Xu, A. Liu, Y. Xu, C. Yan, Experimental study on a new gas–liquid separator for a wide range of gas volume fraction, Chem. Eng. Res. Des. 160 (2020) 561–570.
[30] L.L. Vasiliev, Heat pipes in modern heat exchangers, Appl. Therm. Eng. 25 (2005) 1–19.
[31] C. Wen, H. Ding, Y. Yang, Optimisation study of a supersonic separator considering nonequilibrium condensation behaviour, Energy Convers. Manag. 222 (2020) 113210.
[32] S.F. Interlenghi, F.S. Raquel De Pádua, J.L. de Medeiros, O.D.Q.F. Araújo, Low-emission offshore Gas-To-Wire from natural gas with carbon dioxide: Supersonic separator conditioning and post-combustion decarbonation, Energy Convers. Manag. 195 (2019) 1334–1349.
[33] H. Ding, C. Sun, C. Wen, Z. Liang, The droplets and film behaviors in supersonic separator by using three-field two-fluid model with heterogenous condensation, Int. J. Heat Mass Transf. 184 (2022) 122315.
[34] W. Alnoush, M. Castier, Shortcut modeling of natural gas supersonic separation, J. Nat. Gas Sci. Eng. 65 (2019) 284–300.
[35] H. Ding, Y. Zhang, Y. Yang, C. Wen, A modified Euler-Lagrange-Euler approach for modelling homogeneous and heterogeneous condensing droplets and films in supersonic flows, Int. J. Heat Mass Transf. 200 (2023) 123537.
[36] G. Zhang, X. Wang, J. Chen, S. Tang, K. Smołka, M. Majkut, et al., Supersonic nozzle performance prediction considering the homogeneous-heterogeneous coupling spontaneous non-equilibrium condensation, Energy (Oxf.) 284 (2023) 129274.
[37] H. Ding, C. Sun, C. Wang, C. Wen, Y. Tian, Prediction of dehydration performance of supersonic separator based on a multi-fluid model with heterogeneous condensation, Appl. Therm. Eng. 171 (2020) 115074.
[38] H. Ding, Y. Zhang, C. Sun, Y. Yang, C. Wen, Numerical simulation of supersonic condensation flows using Eulerian-Lagrangian and Eulerian wall film models, Energy (Oxf.) 258 (2022) 124833.
[39] C. Wen, X. Cao, Y. Yang, J. Zhang, Swirling effects on the performance of supersonic separators for natural gas separation, Chem. Eng. Technol. 34 (2011) 1575–1580.
[40] D. Hu, Y. Wang, C. Ma, Numerical simulation of supersonic separator with axial or tangential outlet in reflow channel, Chem. Eng. Process. 124 (2018) 109–121.
[41] C. Wen, X. Cao, Y. Yang, W. Li, Numerical simulation of natural gas flows in diffusers for supersonic separators, Energy (Oxf.) 37 (2012) 195–200.
[42] D. Majidi, F. Farhadi, Effect of the wet outlet geometry on the shockwave position in supersonic separators, Chem. Eng. Technol. 43 (2020) 126–136.
[43] C. Wen, Y. Yang, J.H. Walther, K.M. Pang, Y. Feng, Effect of delta wing on the particle flow in a novel gas supersonic separator, Powder Technol. 304 (2016) 261–267.
[44] Y. Yang, A. Li, C. Wen, Optimization of static vanes in a supersonic separator for gas purification, Fuel Process. Technol. 156 (2017) 265–270.
[45] J. Chen, W. Jiang, X. Lai, X. Cao, J. Bian, Z. Bi, Study on the influence of wall-mounted cyclone on the purification and separation performance of supersonic separator, Chem. Eng. Process. 150 (2020) 107898.
[46] H. Ding, Y. Dong, Y. Zhang, C. Wen, Y. Yang, Exergy performance analysis of hydrogen recirculation ejectors exhibiting phase change behaviour in PEMFC applications, ENERGY 300 (2024) 131563.
[47] H. Ounis, G. Ahmadi, J.B. McLaughlin, Brownian diffusion of submicrometer particles in the viscous sublayer, J. Colloid Interface Sci. 143 (1991) 266–277.
[48] O'ROURKE PJ. Collective drop effects on vaporizing liquid sprays: Princeton University; 1981.
[49] A. Kantrowitz, Nucleation in very rapid vapor expansions, J. Chem. Phys. 19 (1951) 1097–1100.
[50] B. Wahdame, D. Candusso, X. François, F. Harel, J. Kauffmann, G. Coquery, Design of experiment techniques for fuel cell characterisation and development, Int. J. Hydrogen Energy 34 (2009) 967–980.
[51] M.M. Rajabi, B. Ataie-Ashtiani, H. Janssen, Efficiency enhancement of optimized Latin hypercube sampling strategies: application to Monte Carlo uncertainty analysis and meta-modeling, Adv. Water Resour. 76 (2015) 127–139.
[52] M.J. Asher, B.F. Croke, A.J. Jakeman, L.J. Peeters, A review of surrogate models and their application to groundwater modeling, Water Resour. Res. 51 (2015) 5957–5973.
[53] F.A. Lucay, M. Sales-Cruz, E.D. Gálvez, L.A. Cisternas, Modeling of the complex behavior through an improved response surface methodology, Miner. Process. Extr. Metall. Rev. 42 (2021) 285–311.
[54] C.C. Coello, Evolutionary multi-objective optimization: A historical view of the field, IEEE Comput. Intell. Mag. 1 (2006) 28–36.
[55] N. Srinivas, K. Deb, Muiltiobjective optimization using nondominated sorting in genetic algorithms, Evol. Comput. 2 (1994) 221–248.

[56] Y. Deng, B. Yu, D. Sun, Multi-objective optimization of guide vanes for axial flow cyclone using CFD, SVM, and NSGA II algorithm, Powder Technol. 373 (2020) 637–646.
[57] M. Guo, D.K. Le, X. Sun, J.Y. Yoon, Multi-objective optimization of a novel vortex finder for performance improvement of cyclone separator, Powder Technol. 410 (2022) 117856.
[58] M. Neagu, D.L. Cursaru, Technical and economic evaluations of the triethylene glycol regeneration processes in natural gas dehydration plants, J. Nat. Gas Sci. Eng. 37 (2017) 327–340.
[59] S. Wang, C. Wang, H. Ding, S. Li, Evaluation of dynamic behaviors in varied swirling flows for high-pressure offshore natural gas supersonic dehydration, Energy (Oxf.) 300 (2024) 131498.